Kim *et al. Energy Mater.* **2025**, *5*, 500072
DOI: 10.20517/energymater.2024.255

Energy Materials

Article

Open Access

Check for updates

Multi-layered yolk-shell design containing carbon bridge connection for alloying anodes in lithium-ion batteries

Donghwi Kim[1,#], S. Jayasubramaniyan[2,#], Seokjin Kim[1], Jueun Kim[1], Minseok Ko[1], Taehong Kim[3], Hooam Yu[3], Hyo-Jun Ahn[3], Kwon-Koo Cho[3], Sang Yong Nam[1,2,*], N. S. Reddy[3,*], Jaekyung Sung[1,3,*]

[1]Department of Materials Engineering and Convergence Technology, Gyeongsang National University, Jinju 52828, Republic of Korea.
[2]Research Institute for Green Energy Convergence Technology, Gyeongsang National University, Jinju, 52828, Republic of Korea.
[3]School of Materials Science and Engineering, Engineering Research Institute, Gyeongsang National University, Jinju 52828, Republic of Korea.
[#]Authors contributed equally.

[*]**Correspondence to:** Dr. Jaekyung Sung, Department of Materials Engineering and Convergence Technology, Gyeongsang National University, jinjudaero 501, Jinju 52828, Republic of Korea. School of Materials Science and Engineering, Engineering Research Institute, Gyeongsang National University, jinjudaero 501, Jinju 52828, Republic of Korea. E-mail: jksung@gnu.ac.kr; Dr. N. S. Reddy, School of Materials Science and Engineering, Engineering Research Institute, Gyeongsang National University, jinjudaero 501, Jinju 52828, Republic of Korea. E-mail: nsreddy@gnu.ac.kr; Dr. Sang Yong Nam, Department of Materials Engineering and Convergence Technology, Gyeongsang National University, jinjudaero 501, Jinju 52828, Republic of Korea. Research Institute for Green Energy Convergence Technology, Gyeongsang National University, jinjudaero 501, Jinju 52828, Republic of Korea. E-mail: walden@gnu.ac.kr

How to cite this article: Kim, D.; Jayasubramaniyan, S.; Kim, S.; Kim, J.; Ko, M.; Kim, T.; Yu, H.; Ahn, H. J.; Cho, K. K.; Nam, S. Y.; Reddy, N. S.; Sung, J. Multi-layered yolk-shell design containing carbon bridge connection for alloying anodes in lithium-ion batteries. *Energy Mater.* **2025**, *5*, 500072. https://dx.doi.org/10.20517/energymater.2024.255

Received: 15 Nov 2024 **First Decision:** 21 Jan 2025 **Revised:** 6 Feb 2025 **Accepted:** 10 Feb 2024 **Published:** 12 Mar 2025

Academic Editor: Sen Xin **Copy Editor:** Ping Zhang **Production Editor:** Ping Zhang

Abstract

Designing a material structure that supports high-capacity and long cycle life in silicon (Si) anodes has been a long-standing challenge for advancing lithium-ion batteries. Yolk-shell design has been considered a most promising design for alleviating the volume expansion feature of Si. However, the significant void between the Si core and the outer shell limits electrical contact and the complete utilization of the Si core and deteriorates the battery performance upon cycling. In this study, we synthesized a bridged multi-layered yolk-shell (MYS) structure design via thermal decomposition of SiH_4 and carbon oxidation in the air atmosphere. This MYS design features a void space to accommodate the volume expansion of the Si core. It includes a carbon bridge (CB) that connects the Si core and outmost shell containing SiO_x/Si/SiO_x which improves the electrical contact and lithiation kinetics of the

Si core and addresses fundamental issues of low contact between core and shell. As a result, the CB-MYS structure exhibits a high specific capacity of 2,802.2 mAh g^{-1}, an initial Coulombic efficiency of 90.0%, and maintains structural integrity and stable cycling performance. Hence, we believe the CB-MYS structure is a promising engineering design to enhance the performance of high-capacity alloy anodes for next-generation lithium-ion batteries.

Keywords: Silicon anode, multi-layered-yolk-shell, carbon bridge, lithiation kinetics, Li-ion battery

INTRODUCTION

The role of high-energy lithium-ion batteries (LIBs) in developing electric vehicles with much longer driving ranges has gained increasing prominence in energy storage technology research[1,2]. The energy density of commercial LIBs with graphite as the anode has been restricted to 200 Wh/kg owing to the limited specific capacity (372 mAh g^{-1}), which limits the further increasing energy density and its application in high-energy LIBs[3,4]. In this context, silicon (Si) with a high theoretical gravimetric capacity of 3,592 mAh g^{-1} has been highlighted as a promising anode, which helps to achieve the energy density of 500 Wh Kg^{-1} and contributes to developing high-energy LIBs[5]. However, its massive volume expansion (300%) brings about severe morphological change and crack formation during cycles, which causes interparticle contact loss and high irreversible capacity originating from continuous consumption of lithium sources. Furthermore, the formation of a thick and unstable solid electrolyte interphase (SEI) layer occurs owing to the exposure of the Si surface to the electrolyte, leading to poor ionic and electrical conductivity and capacity fading. These significant challenging problems with Si anodes limit their application in high-energy LIBs[6,7].

Researchers have utilized various strategies to mitigate the volume expansion-induced challenging issues of Si anodes. For instance, reducing the size of the Si particle from micron to nano-size has been widely investigated to alleviate the volume expansion and reduce the Li^+ ion diffusion path in the Si anode[8,9]. However, downsizing the Si particle increases the active surface area of Si, which promotes the parasitic reaction of Si with electrolyte, thus forming a thick and unstable SEI layer. The thick SEI layer and the formation of insulating by-products prevent Li^+ diffusion and deteriorate the battery performance[10,11]. To address these issues and volume expansion features of Si, nano-structuring strategies such as constructing porous particles[12], nanowires[13], and designing Si/carbon (C) composites[14-16] have been successfully investigated. Graphite and Si are physically blended to produce Si-C composite anodes. Nevertheless, the restricted buffering effect cannot entirely compensate for the volume expansion of Si and direct interaction with the electrolyte leads to interface instability. To address this, Ryu *et al.* reported a molecular-level mixed Si-C composite anode, synthesized via heat pyrolysis of silane and subsequent mechanical milling. During cycling, electrochemical dissociation and reclustering of disordered Si-C bonds occur and the compact Si architecture inhibits detrimental electrochemical aggregation and direct interaction with the liquid electrolyte, hence stabilizing surfaces. Despite lacking extra void spaces for Si expansion, the Si-C composites developed here exhibited reduced electrode swelling, meeting practical standards while extending battery cycle life[17].

The core-shell design with rigid surface coating on Si particles has been widely used to alleviate the volume expansion of Si and minimize the parasitic reaction with organic electrolytes[18-22]. For instance, Yu *et al.* demonstrated that TiN functioned as a selective blocking layer exhibiting high conductivity and specific selectivity for fluoride anions on the Si surface, successfully inhibiting fluoride anion infiltration. This protective layer significantly reduces the side reaction rate by a factor of 1,700 and the SEI thickness by a factor of four. The Si@TiN core-shell anode exhibits a high lithium-ion diffusion coefficient and a very low

Coulombic inefficiency of merely 0.01% per cycle in the slow decay phase at a current density of 0.5 A g^{-1}. However, the structural integrity of Si was not maintained due to the rigidness of the coating layer, which continuously breaks during the volume expansion[23].

Yolk-shell designs with void space have been spotlighted as a viable engineering design, which offers enough space to accommodate the Si volume expansion. For instance, Liu *et al.* reported that the yolk-shell design of Si@void@C exhibited high cycle stability and the in-situ transmission electron microscopy (TEM) analysis revealed that the well-defined void space allows the Si particles to expand without breaking the carbon shell, maintains the electrical contact, and helps stabilize the SEI layer[24]. Moreover, the advantages and effectiveness of the yolk-shell design in achieving high performance using Si anodes have been confirmed in many subsequent literature reports[25-27]. Recently, Du *et al.* developed a distinctive ternary composite anode material (Si/Cr_2O_3/C), whereby Si nanoparticles (SiNPs) are encapsulated within carbon-coated chromium oxide multishell hollow spheres (MSHSs). This encapsulation significantly improves cyclability by allowing free room for volume changes while maintaining the structural integrity of the Cr_2O_3/C hybrid matrix. The designed Si/Cr_2O_3/C composite anode has a substantial reversible capacity of 1,351 mA h g^{-1} at 100 mA g^{-1} and exhibits remarkable cycling stability, maintaining 716 mA h g^{-1} after 300 cycles at 500 mA g^{-1}[28]. However, the electrochemical performance of the yolk-shell design deteriorated due to a few significant challenges, including the lack of point-to-point electrical contact between Si yolk and the outer shell and corrosion of Si yolks due to the side reaction with the penetrated organic electrolyte. It shows a relatively lower specific capacity compared to the theoretical capacity of Si because of the shells with non-active materials (i.e., not accompanying electrochemical de-lithiation for capacity). Furthermore, the persistence of empty void space reduces the volumetric energy density of the cell, and it is vulnerable to mechanical stress derived from the electrode calendering process[29,30]. Moreover, the nano-sized yolk-shell Si particle exposed a larger surface area, resulting in severe side reactions with electrolytes, low tab density, and high interparticle resistance, which led to the hindrance for the practical application.

Herein, we propose the synthesis of a carbon bridged (CB) multi-layered yolk-shell (MYS) structure with Si yolk, void space, rigid outer multishell containing SiO_x/Si/SiO_x, and the carbon connecting bridge between SiNP yolk and outmost shell *via* thermal decomposition of SiH_4 gases followed by carbon oxidation under the air atmosphere. The material design in this study provides several attractive advantages. First, the CB connecting the SiNPs and SiO_x/Si/SiO_x shells gives high electric and ionic conductivity and addresses fundamental issues of low point-to-point contact between the outer SiO_x/Si/SiO_x multishell and Si particle in the yolk-shell structure. Second, systemically designed void space helps to accommodate the volume expansion of SiNPs. Third, the SiO_x/Si/SiO_x multishell acts as a protective layer to minimize the direct interaction of organic electrolytes with the Si surface, stabilizing the SEI layer and preventing undesired by-products on the anode surface during cycles. Also, the Si in the multishell further increases the specific capacity, and the robustness of the multilayer helps to attain more structural integrity even after the calendering process and minimizes particle pulverization. Finally, the synthesis method demonstrates industrial applicability by flowing gases step by step, simplifying the single-batch process, and producing secondary particles during the decomposition of C_2H_2. Specifically, these secondary particle CB-MYS structures with relatively low specific surface area lead to a high initial Coulombic efficiency (CE) and increase the tap density. As a result, MYS demonstrates a high specific capacity of 2,802.2 mAh g^{-1}, an initial CE of 90.0%, and maintains particle integrity and stable cycling performance even after 50 cycles without any significant changes in the electrode thickness.

EXPERIMENTAL

Synthesis of CB-MYS

First, we synthesized carbon-coated SiNP (SiNP@C) through a chemical vapor deposition (CVD) process. The CVD method was selected for Si and C coating because it produces uniform, thin, high-quality coatings with excellent adhesion. The commercial SiNPs were loaded into the customized stainless steel (SUS)-tube furnace, and high-purity N_2 balanced/10 mol% acetylene gas (C_2H_2) flowed into the tube furnace at 900 °C with a flow rate of 0.05 L min^{-1} for 60 and 120 min to form a thin and thick carbon coating layer on the Si, respectively. Then, Si coating on SiNP@C to form a MYS structure of SiNP@C@Si was performed by flowing the high-purity silane gas (SiH_4, 99.9%) into the same CVD furnace at 475 °C with a flow rate of 0.1 L min^{-1} for 60 min. The thermal decomposition of SiH_4 gas forms a uniform and thin Si coating layer. Then, a CB MYS design (CB-MYS) was obtained through thermal etching of the carbon layer in the air atmosphere. The obtained SiNP@C@Si sample was calcinated in a tube furnace under the air atmosphere at 600 °C, 700 °C, 800 °C, and 900 °C to perform thermal etching. The partial and complete oxidation of the carbon shell forms the MYS structure with a CB and well-defined void space, respectively. In addition, the calcination step in the air atmosphere also performs the Si surface oxidation from the SiO_x layer on the Si surface with different thicknesses depending on the calcination temperature, thus forming the outer shell with SiO_x/Si/SiO_x configuration.

Material characterization

The structural and morphological features of the synthesized materials were investigated using scanning electron microscopy (SEM, Verios 460, FEI), high-resolution TEM (HR-TEM, Helios 450HP, FEI), and X-ray diffraction (XRD) analysis (D/MAZX 2500V/PC, Rigaku). Further, cross-sectional SEM analysis was performed to investigate the changes in the electrode thickness and morphological stability of SiNP and MYS structure after 50 galvanostatic charge-discharge cycles (GCD). The coin cells were disassembled inside the Ar-filled glow box after 50 GCD cycles, and the cycled electrode was thoroughly rinsed using a dimethyl carbonate (DMC) solvent. The obtained electrode was subjected to the ion milling process (IM-40000, Hitachi) before the cross-sectional SEM analysis.

Electrochemical characterization

The half-cell electrochemical performance of the obtained samples was investigated by preparing the electrode slurry consisting of active material (SiNP, SiNP@C@Si, CB-MYS 600, CB-MYS 700, and MYS 800), binder [Styrene Butadiene Rubber-SBR (Zeon), Sodium Carboxymethyl Cellulose-CMC (Nippon paper)], and conductive agent (Super P, TIMCAL) in a mass ratio of 90:2.5:2.5:5. The obtained electrode slurry was cast on the copper foil (Cu) collect collecter with a mass loading in the range of 1.0~1.5 mg cm^{-2} and dried in the vacuum oven at 80 °C for 12 h to remove the solvent. Then, the electrode foil was calendered between SS plates to maximize the electrode density. The CB-MYS 600/Gra sample was prepared for the practical demonstration by blending the 10 wt% of CB-MYS 600 and 90 wt% of commercial graphite using a ball mill. The 10 wt% CB-MYS 600 electrode slurry was prepared by a similar procedure described earlier. For rate rest comparison, SiNP/Gra and MYS800/Gra electrodes were prepared with similar conditions. Then, the CR-2023-coin cell was assembled for the half-cell test inside the glove box, where oxygen (O_2) and moisture (H_2O) levels were maintained under 0.5 ppm. Lithium metal foil (Honjo metal) and microporous polyethylene (20 μm, celgard) were used as the counter electrode and separator during the cell assembly. The half-cell electrochemical performance was investigated in the working potential between 0.01 V and 1.5 V at 0.5 C-rate using a battery cycler (TOYO SYSTEM). In this study, all the electrochemical experiments were conducted in temperature-controlled isothermal chambers.

RESULTS AND DISCUSSION

The synthesis of CB-MYS and MYS structure was achieved through a CVD process by using various gases (SiH_4, C_2H_2) with subsequent calcination in the air atmosphere, as depicted in Figure 1A. Initially, SiNPs were loaded onto a tube furnace, and carbon coating on the SiNPs was conducted by using C_2H_2 at 900 °C to produce the SiNP@C. Notably, primary SiNP particles build up the secondary particles during this excessive carbon coating synthesis. Then, the Si@C@SiNP design was achieved via the thermal decomposition of SiH_4 in which the Si nano-layer is coated on the SiNP@C at 475 °C. Carbon oxidation was conducted by blowing air into the furnace at 600 °C and 800 °C. At 600 °C, the carbon layer can be partially oxidized, which leads to the formation of the void space to accommodate the volume expansion of SiNPs. Interestingly, the partial oxidation of the carbon layer resulted in a CB, which electrically connects SiNPs and outer SiO_x/Si/SiO_x shells. At 800 °C, the carbon layer oxidized completely, forming a void space without a CB between the Si core and SiO_x/Si/SiO_x shells. The distinct functions of each part, including the Si inner layer, SiO_x outer layer, CB, void space, and secondary particle, are illustrated in Figure 1B.

To investigate the successful formation of the CB-MYS design and its structural integrity, scanning electron microscopy (SEM) analysis was performed [Figure 1C-F]. We used the commercial SiNPs as starting materials with a diameter of 50 nm, and homogenously distributed primary SiNPs on the Si wafer substrate were observed, as shown in Figure 1C. The CVD-assisted carbon coating was carried out to produce the carbon sacrificial template for creating the void space and CB, and the carbon content and thickness of the coating layer were controlled through the CVD time. There are several reasons for adopting the CVD method for carbon and Si coating in this study. First, void space with a constant gap between the SiNP yolk and the outer shell layer is a prerequisite for the yolk-shell structure. Thus, it is necessary to have a conformal and uniform sacrificial carbon template layer on the surface of SiNPs[31-33]. Compared with a solution-based coating such as sol-gel, uniform and thin layer coating can be realized through the CVD-assisted gas phase coating. Secondly, the multishell coating can be accomplished through a single CVD process by altering the precursor gases at each sequential stage[34]. The conformal and uniform carbon coating on Si through the CVD process was confirmed by the SEM images of SiNP@C [Figure 1D]. After carbon coating, the spherical shape of the Si particle was well preserved, and an increase in the particle size (~150 nm) was observed owing to the persistence of the carbon layer. Interestingly, the primary SiNPs built up secondary particles (< 50 μm) by connecting via the carbon layer, which was formed during the CVD process [Figure 2A-D]. The formation of secondary particles with nanosized Si domains will increase the tapped density[35]. Further, we increased the CVD process time to generate an excessive carbon layer on the Si (SiNP@EC), which further increased the primary particle size (~250 nm) and secondary particles (> 50 μm), as shown in Figure 2E and F. The comparison of primary particle size of SiNP, SiNP@C, and SiNP@EC is demonstrated in Figure 2G. In addition, the persistence of an excessive carbon layer is not desirable because it can form a large void space between the Si yolk and outer shell after the thermal etching process which will increase electric pathway and Li^+ diffusion length[36]. Therefore, we selected SiNP@C for designing the CB-MYS structure. Furthermore, we performed a simple mathematical calculation to calculate the expected size of SiNP after the complete lithiation based on the 300% volume expansion. The calculation results showed that the size of expanded SiNP was ~80 nm after lithiation [Figure 2H].

To fabricate the CB-MYS, carbon oxidation of SiNP@C@Si was conducted at a different temperature range from 600 °C to 900 °C. The temperature range was chosen with consideration of carbon oxidation temperature (> 500 °C) and silicon oxidation temperature (> 700 °C). The weight ratio of the SiNP@C@Si showed a decreasing trend until reaching 700 °C and then increased until 900 °C, indicating that carbon oxidation was predominant until 700 °C and Si oxidation was predominant above 700 °C [Figure 3A]. Consequently, as shown in SEM images of Supplementary Figure 1, the samples calcined at 600 °C and

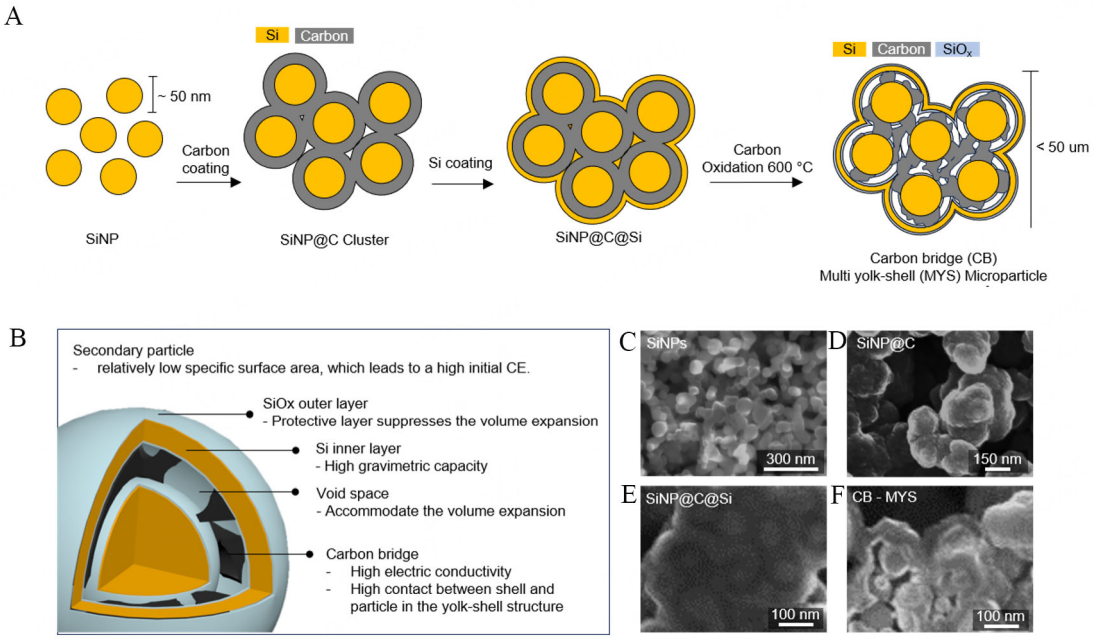

Figure 1. Schematic of fabrication and characteristics of the multi-layered yolk-shell (MYS). (A) Schematic of the fabrication process for the MYS; (B) Cross-sectional schematic view showing the detailed structural characteristics of the Carbon bridge (CB) MYS; SEM images of (C) SiNP; (D) SiNP@C; (E) SiNP@C@Si; and (F) CB-MYS. SEM: Scanning electron microscopy.

700 °C exhibit CB-MYS structures, where the void space between Si yolk and the outer shells is less distinct. In contrast, we observed well-definesd void space with MYS structure for the 800 °C calcined sample owing to the complete oxidation of the carbon coating layer[37]. These observations indicate that partial oxidation of carbon was observed for the 600 °C and 700 °C, which could form the CB connection between the core and outer shell, validating the formation of the CB-MYS structure. In addition, we also observed charging phenomena in the SEM images, which might have originated from the formation of the SiO_x ($0 < x < 2$). It is well known that such SiO_x ($0 < x < 2$) is generated on Si during the calcination in an air atmosphere at the temperature ranges 500~700 °C, acts as a protective layer suppressing volume expansion of Si, and suppresses the side reaction of Si surface with organic electrolyte[38]. Nevertheless, high oxidation temperatures such as 800 °C could produce the excessive formation of SiO_x ($0 < x < 2$) and large amounts of Si oxide (SiO_2), which is not favorable for achieving good electrochemical performance with Si anodes[39].

To further investigate the structure of CB-MYS, we used TEM to observe the morphology of SiNP@C@Si and different temperature calcined samples. As shown in Figure 3B-D, a carbon layer with a thickness of 30~50 nm is observed in between the crystalline SiNP yolk and the outer amorphous Si shell (~20nm) for the SiNP@C@Si. These observations are well-matched with SEM results of Si@C. Notably, we observed the presence of a CB and void space between the SiNP yolk and Si shells for the sample calcined at 600 °C, which originates from the partial oxidation of the carbon layer at 600 °C [Figure 3E-G]. This partial oxidation leaves the residue carbon network, which bridges the core and shell. When the calcination temperature was increased to 700 °C, increased carbon oxidation was observed, which reduced the connections between the core and outer shell, leading to low electronic conductivity, resulting in a typical yolk-shell structure [Figure 3H-J]. Consequently, we observed a complete yolk shell for the 800 °C owing to the complete oxidation of the carbon interlayer due to the high temperature. The complete oxidation process causes complete degradation of the bridge connection, leading to the formation of well-defined void space between the Si yolk and outer shell [Figure 3K-M]. In addition, the high temperature leads to the

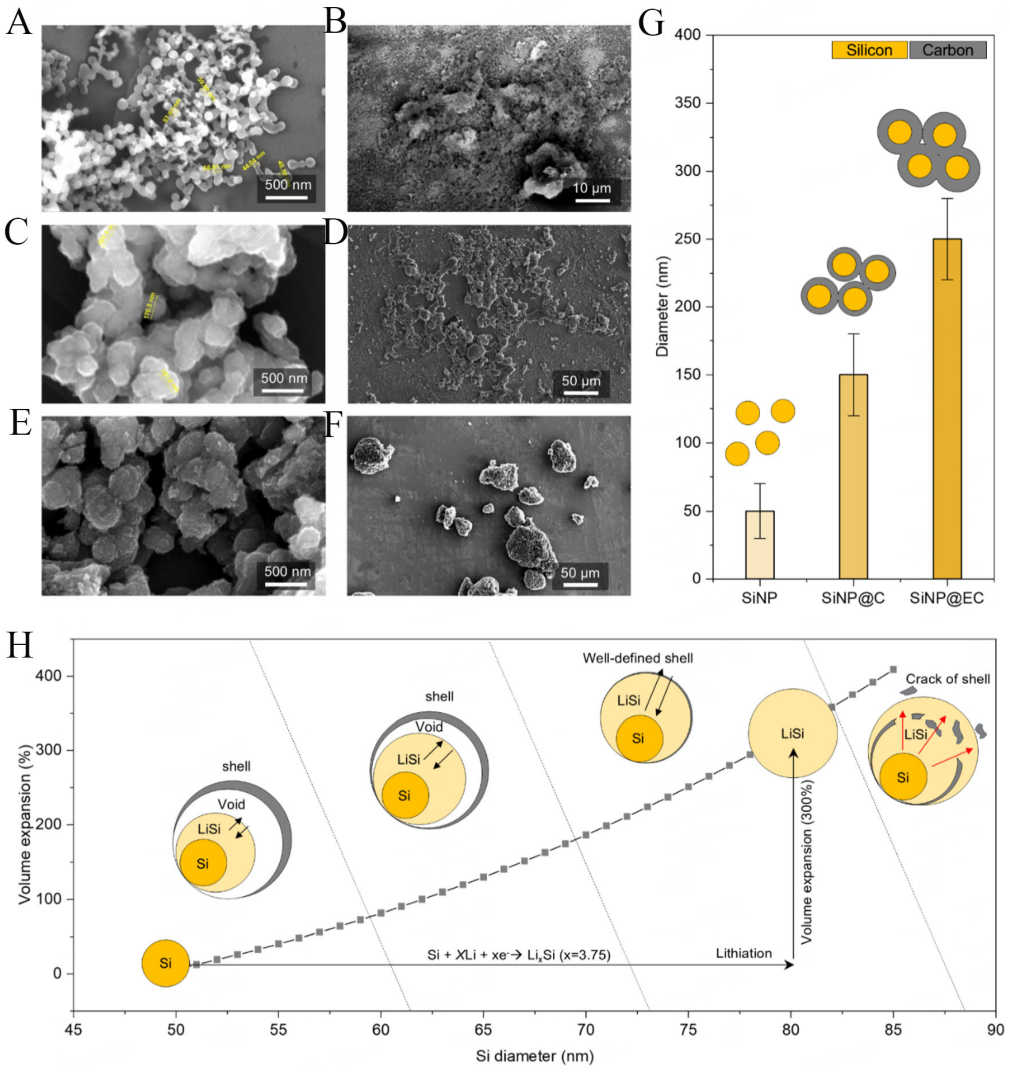

Figure 2. Investigating the size and morphology according to carbon coating. Top-view of the SEM images of (A and B) SiNPs; (C and D) SiNP@C; and (E and F) SiNP@EC; (G) The comparison of primary particle size of each SiNP, SiNP@C, and SiNP@EC; (H) The simple mathematical calculation of 300% volumetric expanded primary particle size of SiNP. SEM: Scanning electron microscopy.

formation of a thick SiO_x ($0 < x < 2$) layer with a thickness of > 3 nm on both surfaces of SiNP yolk and shells during carbon oxidation, which leads to gravimetric capacity loss and low electric and ionic conductivity[40]. As a result, we believe that the carbon oxidation temperature of 600 °C is more suitable for designing the CB-MYS structure with the proper amount of void space and CB to accommodate the volume expansion of Si and enhance the electronic and ionic transport between the shell and yolk. From this point forward, samples calcined at 600 °C, 700 °C, and 800 °C will be designated as CB-MYS-600, CB-MYS-700, and MYS-800, respectively.

To further validate the existence of crystalline and amorphous Si in CB-MYS 600, XRD analysis was performed [Supplementary Figure 2A]. The existence of well-defined XRD peaks confirmed the existence of crystalline Si and the observed broad peak indicates the presence of amorphous Si which coincided with TEM analysis results. To further validate the structural design features of CB-MYS, the cross-sectional SEM analysis of SiNP@C@Si, CB-MYS 600, and MYS 800 samples after the focused ion beam (FIB) process was

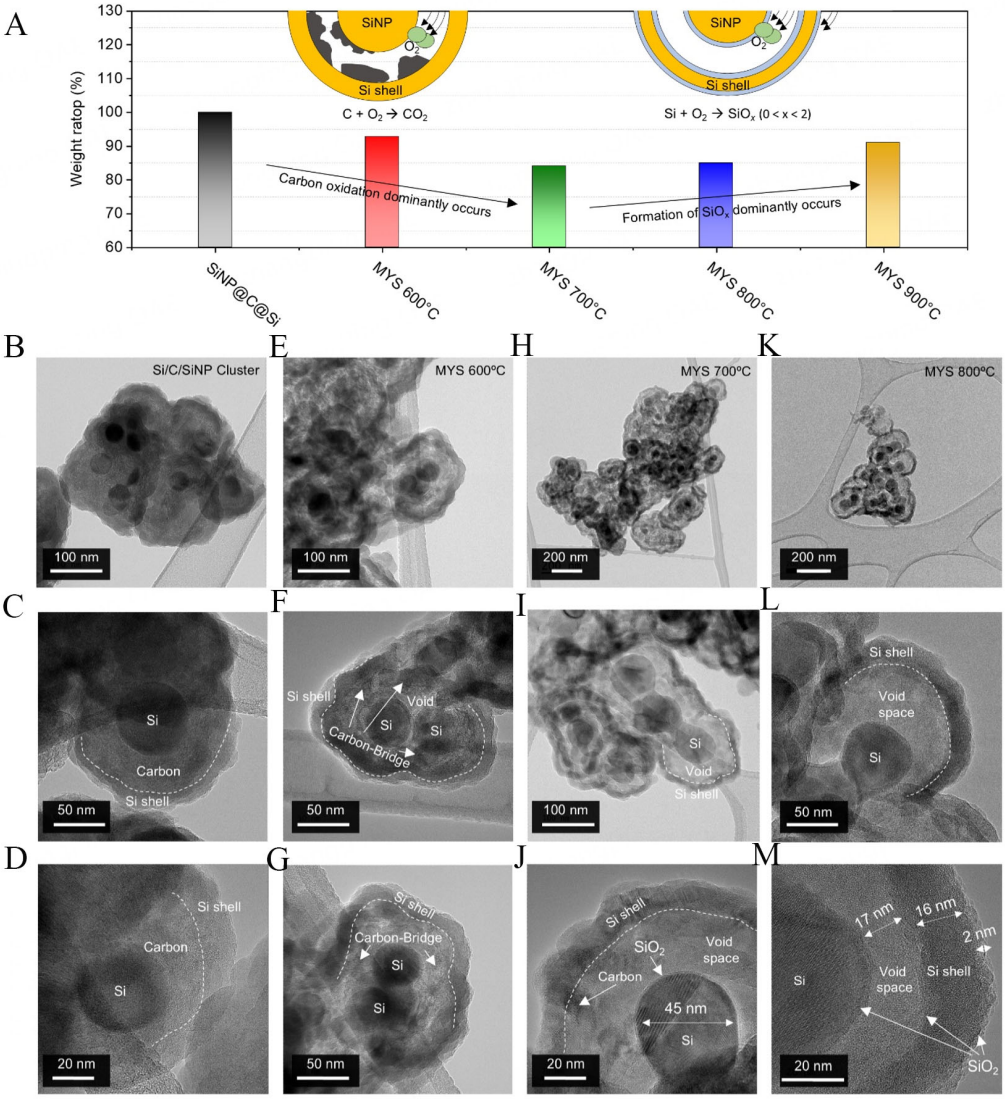

Figure 3. Characteristic change according to heat treatment temperature. (A) The weight ratio of the SiNP@C@Si started to decrease until 700 °C and then increased until 900 °C; TEM images of (B-D) SiNP@C@Si; (E-G) 600 °C; (H-J) 700 °C and (K-M) 800 °C. TEM: Transmission electron microscopy.

investigated [Figure 1E and F, Supplementary Figure 2B]. We observed that the carbon layer fully occupied the space between the Si yolk and the outer shell in SiNP@C@Si. In contrast, an empty void space was observed between the Si yolk and the outer shell layer for the MYS 800, owing to the complete oxidation of carbon at 800 °C. Interestingly, we observed the existence of a CB and partial void space between SiNP yolk and Si outer shells for the CB-MYS 600. As a result, we expect that both CB and void space could improve the overall electrochemical performance of CB-MYS 600.

To verify the favorable effect of the CB-MYS 600, we investigated the electrochemical performance of each sample (SiNP@C@Si, CB-MYS 600, CB-MYS 700, and MYS 800) using a coin-type half-cell at 25 °C. The obtained voltage profiles of the initial cycle of each sample are shown in Figure 4A. The observed specific capacity and Initial CE (ICE) of each sample are depicted in Figure 4B. The observed increasing trend in the specific capacity value for the CB-MYS 600 and CB-MYS 700 sample can be attributed to the increasing the

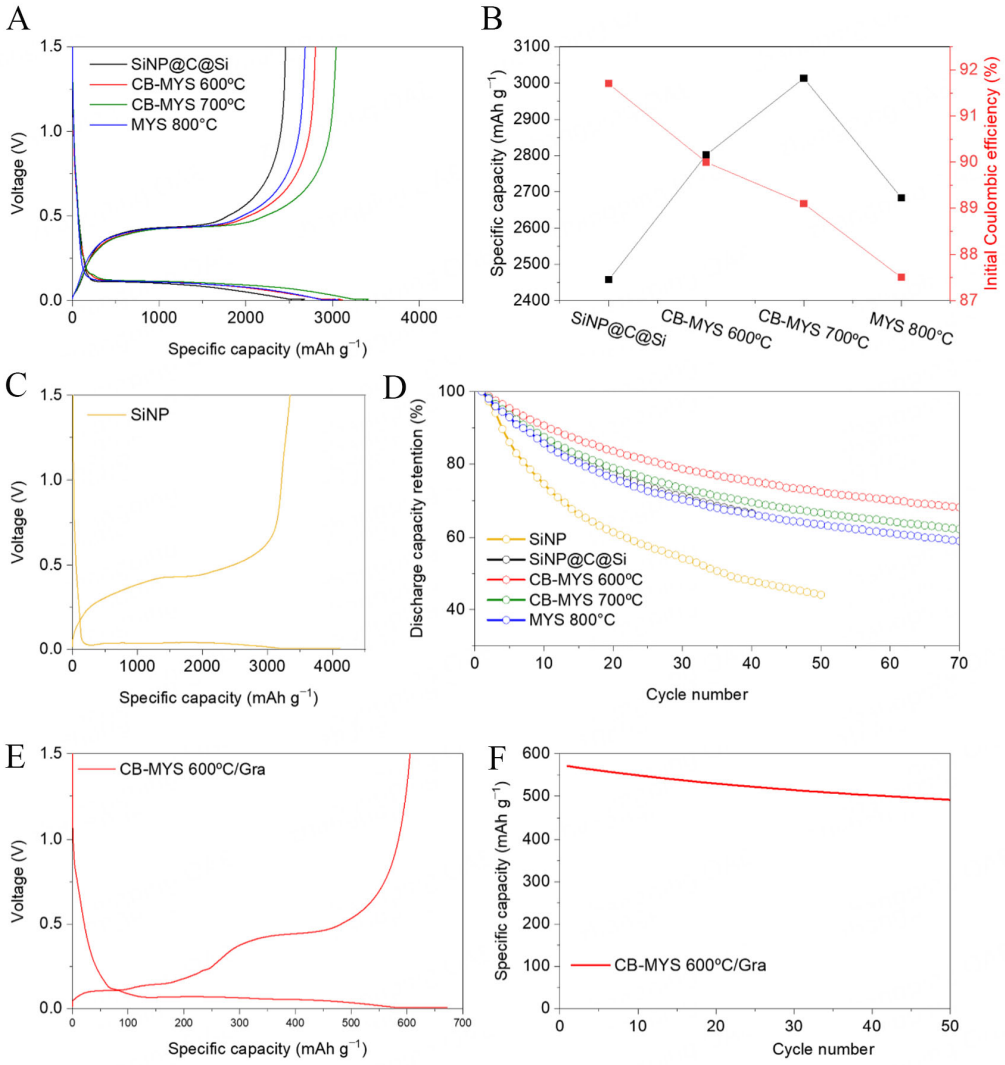

Figure 4. Electrochemical characterization of various anodes: (A) Voltage profiles of SiNP@C@Si, CB-MYS 600, CB-MYS 700, and MYS 800; (B) Specific capacity of SiNP@C@Si, CB-MYS 600, CB-MYS 700, and MYS 800 and their initial Coulombic efficiency; (C) Voltage profiles of SiNP; (D) Discharging capacity retentions of SiNP, SiNP@C@Si, CB-MYS 600, CB-MYS 700, and MYS 800; (E) Voltage profile of the composite containing graphite blended with 10 wt% CB-MYS 600; (F) Discharge capacity of graphite blended with 10 wt% CB-MYS 600. CB: Carbon bridged; MYS: multi-layered yolk-shell.

specific surface area of void space caused by the increase in the carbon oxidation, which leads to formation of a substantial amount of SEI. Further, increased carbon oxidation temperature (MYS 800) displayed a lower specific capacity than other samples due to an excess SiO_x layer formation on the Si surface at high temperatures[41]. The observed ICE values of SiNP@C@Si, CB-MYS 600, CB-MYS 700, and MYS 800 are 91.7%, 90.0%, 89.1%, and 87.5%, respectively. It is observed that the ICE values showed a decreasing trend as the carbon oxidation increased. This observed feature could be ascribed to excessive SiO_x layer formation on the Si surface, which consumes more Li^+ ions during the first cycle and leads to the formation of irreversible and electrochemically inactive by-products such as Li_2O and Li_4SiO_4 on the Si surface[42].

To substantiate the cycling performance of CB-MYS, we also prepared SiNP as a reference sample and compared it to SiNP@C@Si, CB-MYS 600, CB-MYS 700, and MYS 800 [Figure 4C and D]. In this context, the initial CE of SiNP was 81.4%, significantly lower than that of SiNP@C@Si and other MYS samples. This

phenomenon can be attributed to the fact that MYS consists of secondary particles with a relatively low specific surface area. In contrast, SiNP exhibits a high specific surface area, which consumes more active Li^+ ions during SEI formation. Further, we observed all of the treated samples (SiNP@C@Si, CB-MYS 600, CB-MYS 700, and MYS 800) have better cycling stability than that of SiNP, implying that the carbon shell and SiO_x shell acted as a protective layer to stabilize the SiNP anode regardless of the existence of void space [Figure 4D]. Furthermore, SiNP@C@Si and MYS 800 showed similar capacity retention characteristics. The existence of carbon interlayers in the SiNP@C@Si provides high electrical conductivity by connecting SiNP yolk and Si shells and reduces surface exposure to the electrolyte, minimizing by-product formation. However, the absence of void space that accommodates the Si volume expansion induces mechanical crack propagation, which deteriorates the long-term cycle performance[43]. In the case of the MYS 800, void space accommodates the volume expansion feature Si, and the SiO_x layer prevents the side reaction and reduces the formation of by-products. However, due to the persistence of well-defined void space, the electrical isolation of the yolk and outer shell deteriorates the long-cycle performance. Furthermore, to improve the electrical conductivity between CB-MYS particles, carbon nanotubes (CNT) were incorporated as a conductive agent, and the electrochemical performance is represented in Supplementary Figure 3. The CB-MYS 600 CNT electrode exhibited a high ICE (90.01%) and improved cycle stability of 98.4% after 50 cycles, demonstrating superior electrochemical performance compared to the previously reported studies. These results demonstrate that void space and electrical contact between the yolk and the outer shell are essential for achieving stable cycle performance. Interestingly, benefiting from the existence of a CB and void space in the CB-MYS 600 enables the achievement of stable cycle performance. Further, to demonstrate the practical feasibility of CB-MYS 600 anode, we fabricated the electrode containing graphite blended with 10 wt% CB-MYS 600 [Figure 4E]. It showed stable cycling stability and capacity retention of 85.5% for 50 cycles [Figure 4F]. Additionally, to evaluate the high-rate feasibility of the CB-MYS structure, we performed a rate capability test on the SiNP/Gr, CB-MYS 600/Gra, and MYS 800/Gra electrodes [Supplementary Figure 4]. Among these, the CB-MYS 600/Gra electrode demonstrated superior rate performance and higher capacity retention compared to the other electrodes. This enhancement is attributed to the existence of a CB and void space in CB-MYS 600, which facilitates fast lithium-ion diffusion and improves structural stability.

Further, to verify the structural stability of the composite electrode, SEM analysis was performed before and after cycles for the composite electrode and the SEM images showed almost similar morphology before and after 50 cycles which validates the structural integrity of the composite electrode [Supplementary Figure 5]. Additionally, to verify the long-term cycle stability and structural integrity of the CB-MYS 600, post-cycling analysis was conducted to observe the changes in morphology and thickness after 50 cycles using cross-sectional SEM images. We observed vast changes in the thickness of the SiNP electrode after 50 cycles [Figure 5A and B]. The observed electrode expansion ratio was 36% (the thickness of the pristine electrode and the cycled electrode was 22 μm and 30 μm, respectively), and a significant crack was also observed. The vast increase in the electrode thickness and the observed crack in the electrode is owing to the significant volume expansion feature of the SiNPs. In contrast, the CB-MYS 600 electrode exhibited almost no significant change in electrode thickness after 50 cycles [Figure 5C and D]. Further, the magnified SEM images of the electrode particle were investigated to study the morphological changes of particles after cycling. We observed a severe particle crack and morphological changes of SiNP and its initial spherical shape, as presented in Figure 2A, is transformed into spider-web-shaped morphology after 50 cycles [Figure 5E]. In contrast, in the case of CB-MYS 600, although the SiNPs may undergo pulverization, they remain enclosed within the outermost containing SiO_x/Si/SiO_x, preserving its morphological integrity and preventing severe electrical contact loss in the electrode [Figure 5F]. Overall, the existence of the CB and void space in the CB-MYS 600 helps to achieve long-cycle stability and enhance structural stability.

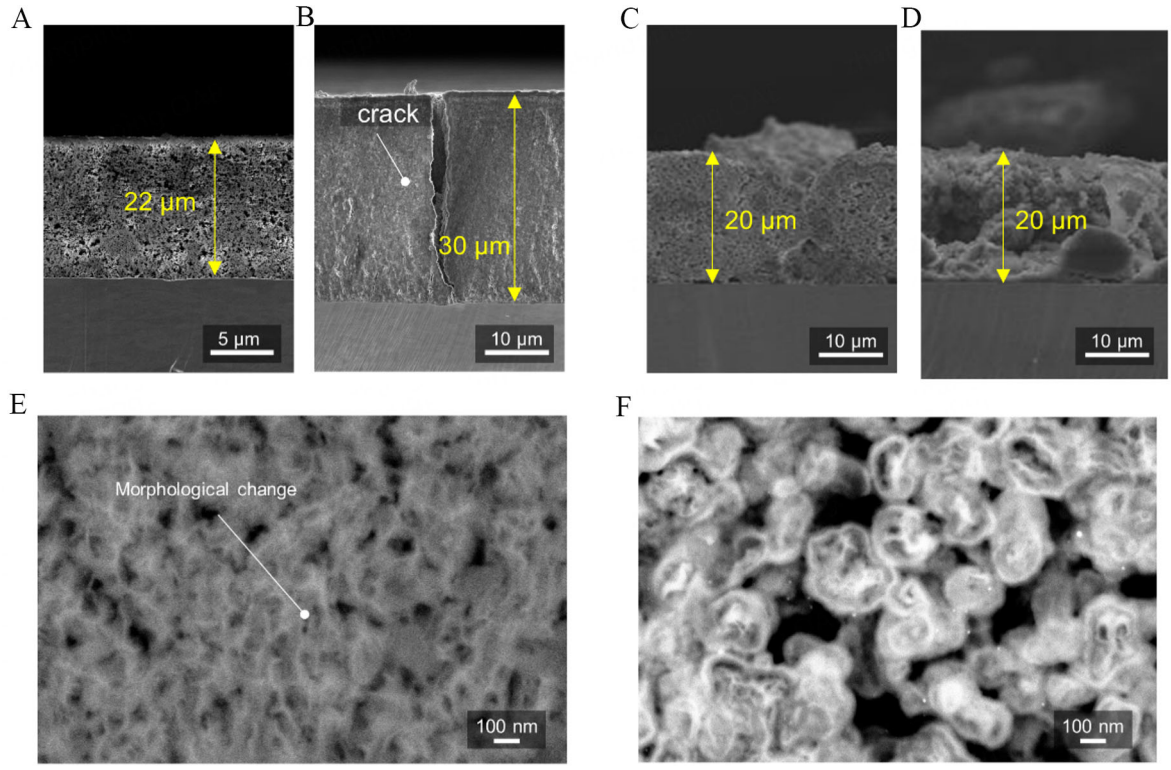

Figure 5. Cross-sectional SEM images for electrode changes before and after. Electrode thickness changes of (A and B) SiNP and (C and D) CB-MYS 600 before and after 50 cycles; Cross-sectional SEM images of (E) SiNP and (F) CB-MYS 600 after 50 cycles. CB: Carbon bridged; MYS: multi-layered yolk-shell; SEM: scanning electron microscopy.

CONCLUSIONS

In summary, we successfully synthesized a bridged MYS structure design via thermal decomposition of SiH_4 and carbon oxidation in the air atmosphere. The SEM and TEM investigation results have confirmed that the MYS consists of void space for accommodating the volume expansion of the Si core and the presence of a CB for connecting the Si yolk and outmost shell containing SiO_x/Si/SiO_x to improve the lithiation kinetics of Si yolk and maintain the electrical contact. As a result, we observed improved electrochemical performance for the CB-MYS structure with a high specific capacity of 2,802.2 mAh g^{-1}, an initial CE of 90.0%, and maintained particle integrity and stable cycling performance without any significant changes change in the electrode thickness after 50 cycles. Therefore, we highlighted that designing the CB-MYS structure is a promising way to enhance the Si anode performance for the application in next-generation LIBs.

DECLARATIONS

Author's contribution

Conceptualization, methodology, writing-original draft: Kim, D.; Jayasubramaniyan, S.
Methodology, investigation, validation, formal analysis: Kim, S.; Kim, J.; Ko, M.
Investigation, validation, writing-review and editing: Kim, T.; Yu, H.; Ahn, H. J.; Cho, K. K.
Validation, funding acquisition, supervision, writing-review and editing: Nam, S. Y.; Reddy, N. S.; Sung, J.

Availability of data and materials

The data are available upon request from the authors.

Financial support and sponsorship

This research was supported by the Basic Science Research Program through the National Research Foundation of Korea (NRF), funded by the Ministry of Education (2020R1A6A03038697). This work was supported by the NRF grant funded by the government of Korea (MSIT) (IRIS RS-2024-00352303). This work was supported by the Technology Innovation Program (RS-2024-00432013) funded By the Ministry of Trade, Industry & Energy (MOTIE, South Korea). This research was supported by Learning & Academic research institution for Master's·PhD students, and Postdocs (LAMP) Program of the NRF grant funded by the Ministry of Education (No. RS-2023-00301974).

Conflicts of interest

All authors declared that there are no conflicts of interest.

Ethical approval and consent to participate

Not applicable.

Consent for publication

Not applicable.

REFERENCES

1. Xu, C.; Behrens, P.; Gasper, P.; et al. Electric vehicle batteries alone could satisfy short-term grid storage demand by as early as 2030. *Nat. Commun.* **2023**, *14*, 119. DOI PubMed PMC
2. Degen, F.; Winter, M.; Bendig, D.; Tübke, J. Energy consumption of current and future production of lithium-ion and post lithium-ion battery cells. *Nat. Energy.* **2023**, *8*, 1284-95. DOI
3. Liu, Y.; Shi, H.; Wu, Z. Recent status, key strategies and challenging perspectives of fast-charging graphite anodes for lithium-ion batteries. *Energy. Environ. Sci.* **2023**, *16*, 4834-71. DOI
4. Asenbauer, J.; Eisenmann, T.; Kuenzel, M.; Kazzazi, A.; Chen, Z.; Bresser, D. The success story of graphite as a lithium-ion anode material - fundamentals, remaining challenges, and recent developments including silicon (oxide) composites. *Sustain. Energy. Fuels.* **2020**, *4*, 5387-416. DOI
5. Sung, J.; Kim, N.; Ma, J.; et al. Subnano-sized silicon anode via crystal growth inhibition mechanism and its application in a prototype battery pack. *Nat. Energy.* **2021**, *6*, 1164-75. DOI
6. Kim, N.; Kim, Y.; Sung, J.; Cho, J. Issues impeding the commercialization of laboratory innovations for energy-dense Si-containing lithium-ion batteries. *Nat. Energy.* **2023**, *8*, 921-33. DOI
7. Kim, M.; Harvey, S. P.; Huey, Z.; et al. A new mechanism of stabilizing SEI of Si anode driven by crosstalk behavior and its potential for developing high performance Si-based batteries. *Energy. Storage. Mater.* **2023**, *55*, 436-44. DOI
8. Lee, Y.; Lee, T.; Hong, J.; et al. Stress relief principle of micron-sized anodes with large volume variation for practical high-energy lithium-ion batteries. *Adv. Funct. Mater.* **2020**, *30*, 2004841. DOI
9. Li, P.; Hwang, J. Y.; Sun, Y. K. Nano/Microstructured silicon-graphite composite anode for high-energy-density Li-ion battery. *ACS. Nano.* **2019**, *13*, 2624-33. DOI PubMed
10. Zhang, X.; Wang, D.; Qiu, X.; et al. Stable high-capacity and high-rate silicon-based lithium battery anodes upon two-dimensional covalent encapsulation. *Nat. Commun.* **2020**, *11*, 3826. DOI PubMed PMC
11. Bärmann, P.; Diehl, M.; Göbel, L.; et al. Impact of the silicon particle size on the pre-lithiation behavior of silicon/carbon composite materials for lithium ion batteries. *J. Power. Sources.* **2020**, *464*, 228224. DOI
12. Kim, B.; Ahn, J.; Oh, Y.; et al. Highly porous carbon-coated silicon nanoparticles with canyon-like surfaces as a high-performance anode material for Li-ion batteries. *J. Mater. Chem. A.* **2018**, *6*, 3028-37. DOI
13. Yang, Y.; Yuan, W.; Kang, W.; et al. A review on silicon nanowire-based anodes for next-generation high-performance lithium-ion batteries from a material-based perspective. *Sustain. Energy. Fuels.* **2020**, *4*, 1577-94. DOI
14. Ma, L.; Fu, X.; Zhao, F.; et al. Microsized silicon/carbon composite anodes through in situ polymerization of phenolic resin onto silicon microparticles for high-performance lithium-ion batteries. *ACS. Appl. Energy. Mater.* **2023**, *6*, 4989-99. DOI
15. Shi, H.; Zhang, W.; Wang, J.; et al. Scalable synthesis of a porous structure silicon/carbon composite decorated with copper as an anode for lithium ion batteries. *Appl. Sur. Sci.* **2023**, *620*, 156843. DOI
16. Son, Y.; Ma, J.; Kim, N.; et al. Quantification of pseudocapacitive contribution in nanocage-shaped silicon-carbon composite anode.

Adv. Energy. Mater. **2019**, *9*, 1803480. DOI

17. Ryu, J.; Bok, T.; Joo, S. H.; et al. Electrochemical scissoring of disordered silicon-carbon composites for high-performance lithium storage. *Energy. Storage. Mater.* **2021**, *36*, 139-46. DOI
18. Li, X.; Zhang, W.; Wang, X.; et al. A stable core-shell Si@SiO_x/C anode produced via the spray and pyrolysis method for lithium-ion batteries. *Front. Chem.* **2022**, *10*, 857036. DOI
19. Yu, C.; Chen, X.; Xiao, Z.; et al. Silicon carbide as a protective layer to stabilize Si-based anodes by inhibiting chemical reactions. *Nano. Lett.* **2019**, *19*, 5124-32. DOI
20. Liu, M.; Gao, H.; Hu, G.; Zhu, K.; Huang, H. Facile preparation of core-shell Si@$Li_4Ti_5O_{12}$ nanocomposite as large-capacity lithium-ion battery anode. *J. Energy. Chem.* **2020**, *40*, 89-98. DOI
21. Casino, S.; Heidrich, B.; Makvandi, A.; et al. Al_2O_3 protective coating on silicon thin film electrodes and its effect on the aging mechanisms of lithium metal and lithium ion cells. *J. Energy. Storage.* **2021**, *44*, 103479. DOI
22. Ngo, D. T.; Le, H. T. T.; Pham, X. M.; Park, C. N.; Park, C. J. Facile Synthesis of Si@SiC composite as an anode material for lithium-ion batteries. *ACS. Appl. Mater. Interfaces.* **2017**, *9*, 32790-800. DOI
23. Yu, C.; Lin, X.; Chen, X.; et al. Suppressing the side reaction by a selective blocking layer to enhance the performance of Si-based anodes. *Nano. Lett.* **2020**, *20*, 5176-84. DOI
24. Liu, N.; Wu, H.; McDowell, M. T.; Yao, Y.; Wang, C.; Cui, Y. A yolk-shell design for stabilized and scalable Li-ion battery alloy anodes. *Nano. Lett.* **2012**, *12*, 3315-21. DOI
25. Luo, H.; Zhang, X.; Xu, C.; et al. Constructing a yolk-shell structure SiO*x*/C@C composite for long-life lithium-ion batteries. *ACS. Appl. Energy. Mater.* **2022**, *5*, 8982-9. DOI
26. Wu, Z.; Luo, J.; Peng, J.; Liu, H.; Chang, B.; Wang, X. Rational architecture design of yolk/double-shells Si-based anode material with double buffering carbon layers for high performance lithium-ion battery. *Green. Energy. Environ.* **2021**, *6*, 517-27. DOI
27. Wang, H.; Que, X.; Liu, Y.; et al. Facile synthesis of yolk-shell structured SiO*x*/C@Void@C nanospheres as anode for lithium-ion batteries. *J. Alloys. Compd.* **2021**, *874*, 159913. DOI
28. Du, H.; Yu, R.; Tan, X.; et al. Encapsulating Si nanoparticles in multi-shell hollow spheres: an effective approach to boost the cyclability. *Sci. China. Mater.* **2023**, *66*, 2199-206. DOI
29. Yao, Y.; Xu, X.; Zhao, H.; Tong, Y.; Li, Y. Multilayer Si@SiO*x*@void@C anode materials synthesized via simultaneously carbonization and redox for Li-ion batteries. *Ceram. Int.* **2022**, *48*, 12217-27. DOI
30. Zhang, L.; Wang, C.; Dou, Y.; et al. A yolk-shell structured silicon anode with superior conductivity and high tap density for full lithium-ion batteries. *Angew. Chem. Int. Ed.* **2019**, *58*, 8824-8. DOI
31. Son, Y.; Kim, N.; Lee, T.; et al. Calendering-compatible macroporous architecture for silicon-graphite composite toward high-energy lithium-ion batteries. *Adv. Mater.* **2020**, *32*, e2003286. DOI
32. Park, S.; Sung, J.; Chae, S.; et al. Scalable synthesis of hollow β-SiC/Si anodes via selective thermal oxidation for lithium-ion batteries. *ACS. Nano.* **2020**, *14*, 11548-57. DOI
33. Chae, S.; Park, S.; Ahn, K.; et al. Gas phase synthesis of amorphous silicon nitride nanoparticles for high-energy LIBs. *Energy. Environ. Sci.* **2020**, *13*, 1212-21. DOI
34. Ko, M.; Chae, S.; Ma, J.; et al. Author correction: scalable synthesis of silicon-nanolayer-embedded graphite for high-energy lithium-ion batteries. *Nat. Energy.* **2020**, *5*, 344-344. DOI
35. Lee, P. K.; Tan, T.; Wang, S.; Kang, W.; Lee, C. S.; Yu, D. Y. W. Robust micron-sized silicon secondary particles anchored by polyimide as high-capacity, high-stability Li-ion battery anode. *ACS. Appl. Mater. Interfaces.* **2018**, *10*, 34132-9. DOI
36. Chae, S.; Ko, M.; Kim, K.; Ahn, K.; Cho, J. Confronting issues of the practical implementation of Si anode in high-energy lithium-ion batteries. *Joule* **2017**, *1*, 47-60. DOI
37. Lu, Y.; Chang, P.; Wang, L.; Nzabahimana, J.; Hu, X. Yolk-shell Si/SiO*x*@Void@C composites as anode materials for lithium-ion batteries. *Funct. Mater. Lett.* **2019**, *12*, 1850094. DOI
38. Xiao, Z.; Yu, C.; Lin, X.; et al. Intrinsic blocking effect of SiO*x* on the side reaction with a $LiPF_6$-based electrolyte. *Catal. Today.* **2021**, *364*, 61-6. DOI
39. Wu, W.; Wang, M.; Wang, J.; Wang, C.; Deng, Y. Green design of Si/SiO_2/C composites as high-performance anodes for lithium-ion batteries. *ACS. Appl. Energy. Mater.* **2020**, *3*, 3884-92. DOI
40. Wu, H.; Zheng, L.; Du, N.; et al. Constructing densely compacted graphite/Si/SiO_2 ternary composite anodes for high-performance Li-ion batteries. *ACS. Appl. Mater. Interfaces.* **2021**, *13*, 22323-31. DOI
41. Wei, H.; Niu, L.; Zhou, X.; et al. Nanostructured SiO*x*/Si composite confined by carbon layer as anode materials for high-performance lithium-ion battery. *J. Alloys. Compd.* **2023**, *969*, 172462. DOI
42. Huang, W.; Wang, J.; Braun, M. R.; et al. Dynamic structure and chemistry of the silicon solid-electrolyte interphase visualized by cryogenic electron microscopy. *Matter* **2019**, *1*, 1232-45. DOI
43. Huang, X.; Guo, R.; Lin, Y.; Cao, Y.; Wu, J. Si/SiC/C in-situ composite microspindles as anode materials for lithium-ion batteries. *Electrochim. Acta.* **2022**, *422*, 140546. DOI